

Open-Structure: a Structural Benchmark Dataset for SLAM Algorithms

Yanyan Li¹, Zhao Guo², Ze Yang², Yanbiao Sun², Liang Zhao³ and Federico Tombari^{1,4}

Abstract—This paper introduces a new benchmark dataset, **Open-Structure**, for evaluating visual odometry and SLAM methods, which directly equips point and line measurements, correspondences, structural associations, and co-visibility factor graphs instead of providing raw images. Based on the proposed benchmark dataset, these 2D or 3D data can be directly input to different stages of SLAM pipelines to avoid the impact of the data preprocessing modules in ablation experiments. First, we propose a dataset generator for real-world and simulated scenarios. In real-world scenes, it maintains the same observations and occlusions as actual feature extraction results. Those generated simulation sequences enhance the dataset’s diversity by introducing various carefully designed trajectories and observations. Second, a SLAM baseline is proposed using our dataset to evaluate widely used modules in camera pose tracking, parametrization, and optimization modules. By evaluating these state-of-the-art algorithms across different scenarios, we discern each module’s strengths and weaknesses within the camera tracking and optimization process. Our dataset and baseline are available at <https://github.com/yanyan-li/Open-Structure>.

I. INTRODUCTION

Camera pose estimation [1]–[3] and scene reconstruction [2], [4]–[6] are pivotal bridges for interaction between robots and unknown environments. These processes enable intelligent agents to determine their location and set the stage for advanced scene comprehension tasks. Recently, general SLAM systems [3], [7], [8] have achieved impressive performances. However, they still have problems in challenging scenarios and sharp camera motions. Algorithms focusing on certain modules, such as structural regularities [9]–[11], parameterization [12], [13], and new optimization loss functions [8], are proposed to improve tracking and mapping performances further. Since these modules cannot directly use raw images during ablation evaluation, different preprocessing steps are required to extract features, correspondences, and even initial factor graphs, which brings uncertain effects into the evaluation process. Since fair and efficient evaluation of these algorithms and modules is a critical step to advance the field, the community has put forward new requirements for datasets, which should be carefully designed to meet the needs of ablation evaluation of visual SLAM methods.

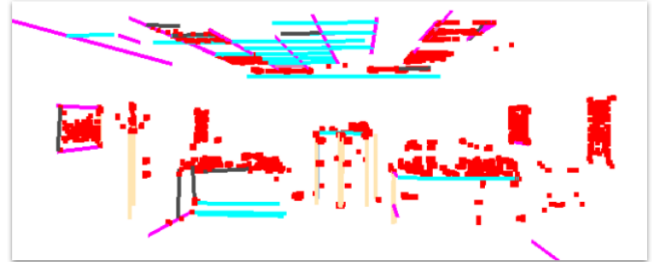
Public datasets [14]–[16] are the basis for promoting the development of SLAM theories, which breaks the dependence of research activities on high-precision hardware

¹Yanyan Li, Federico Tombari are with the Department of Computer Science, Technical University of Munich, Germany

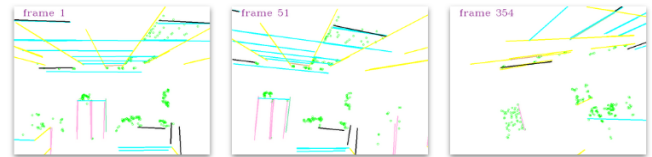
²Zhao Guo, Ze Yang, Yanbiao Sun are with the Tianjin University, China

³Liang Zhao is with School of Mechanical and Mechatronic Engineering, Australia

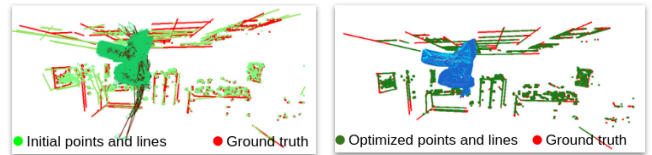
⁴Federico Tombari is with Google, Switzerland.



(a) Ground truth scene. Parallel 3D lines are in the same color.



(b) Measurements of points and structural line segments. Parallel lines are marked in the same color. Black shows individual lines.



(c) Factor graph construction and optimization in the baseline.

Fig. 1: Data provided by Open-Structure Benchmark Dataset are ground truth poses and scenes, 2D measurements, correspondences, structural lines, and co-visibility graphs.

equipment and makes the evaluation process convenient. Generally, we have real-world and synthetic datasets for visual SLAM tasks, where those real-world datasets, such as TUM RGB-D [14], EuRoC MAV [17], and KiTTi [18], are collected in real environments based on elaborate sensor setups. While popular synthetic ones, including ICL-NUIM [15], Virtual-KiTTi [19], and TartanAir [16], are generated from 3D rendering engines by designing virtual scenes and viewpoints. The first type of dataset provides better real-life usage scenarios, but the collection process is expensive, and the properties of the hardware setup also have an impact on the accuracy of the real results. Compared to real-life data, the scene’s realism has decreased in synthetic sequences, but these sequences can flexibly provide multiple types of data formats, such as disparity, normals, and semantics.

Those datasets in raw-image style are suitable for evaluating overall SLAM systems. However, those raw images cannot be directly exploited when we evaluate one of the modules of SLAM systems, like parameterization

approaches. Therefore, several preprocess operations, such as correspondence detection and association, are generally required to extract target information from raw images first. Since ensuring that the preprocess results generated from different SLAM pipelines are the same is complicated, some uncertain effects will be incorporated into ablation studies. Simulation sequences are commonly designed in algorithm comparison to ensure the same inputs are in ablation studies. [20] builds a cube environment with points randomly located on surfaces. The simulated visual observations, acceleration, and gyroscope measurements are used to evaluate on-manifold preintegration approaches for visual-inertial odometry. Occupancy-SLAM [21] designs two simulation scenes with obstacles and robot trajectories to evaluate occupancy map optimization. However, the generation process of these simulation datasets is too simple to simulate real scenarios, with little consideration of real observation relationships and occlusion issues.

To address the problems of those raw-image-based and simulated sequences, this paper introduces a new benchmark dataset, Open-Structure, which contains real-world and simulated sequences. On the one hand, those sequence provides 2D measurements, feature correspondences, structural lines, 3D landmarks, and co-visibility factor graphs, which can be used to evaluate strategies in initial pose estimation, parameterization, optimization, and loop closure modules as shown in Figure 1. On the other hand, observation and occlusion properties are preserved similarly to image-based datasets because our real-world sequences are extended from TUM RGB-D [14], ICL-NUIM [15] and TartanAir [16], and our simulated sequences enhance the dataset’s diversity by introducing various carefully designed trajectories and scenes. Moreover, we provide a baseline architecture that is an incremental tracking and sparse mapping system with different initial pose estimation strategies, point and line representations, and optimization modules. By Feeding our point and line measurements, the baseline can estimate initial camera poses and build a sparse point-line map. Based on the given factor graph data, the baseline implements entrance for testing parameterization and optimization methods. The contributions of this paper are summarized as

- a benchmark dataset containing multiple data formats is provided for evaluating SLAM modules;
- a SLAM baseline is open-sourced to the community, providing tracking and optimization interfaces for using 2D measurements and factor graph data;
- tracking, parameterization, and optimization modules are implemented and evaluated on our benchmark.

II. DATASET FEATURES

As listed in Table I, Open-Structure provides multi-model data, including 2D measurements (points and lines), initial landmarks and poses, structural line associations, and co-visibility factor graphs. Meanwhile, the dataset provides the ground truth of poses and 3D landmarks for evaluating estimated trajectories and reconstruction results.

Data type	Denotation	Equipped
Point measurements	$\mathbf{p} = [\mathbf{p}^T, d]^T$ pixel position and depth	✓
Line measurements	$\mathbf{l} = (\mathbf{p}^s, \mathbf{p}^e)$ start point and end point	✓
Point landmarks	$\mathbf{P}_w = [X_w, Y_w, Z_w]^T$ 3D point in the world coordinate	✓
Line landmarks	$\mathbf{L}_w = (\mathbf{P}_w^s, \mathbf{P}_w^e)$ 3D endpoints in the world coordinate $\mathcal{L}^k = [w_n \mathbf{n}^k \quad w_d \mathbf{d}^k]$ \mathbf{n}^k and \mathbf{d}^k are unit vectors $\mathcal{O}_w = [\phi^T, \varphi]^T$ orthonormal representation	✓
Observations	$\mathbf{P}_w^i = \Pi(\mathbf{p}_{c_k}^j, \mathbf{T}_{w,c_k}, \mathbf{K})$ \mathbf{P}_w^i is observed by camera c_k , intrinsic matrix \mathbf{K}	✓
Correspondences	$\mathbf{c}_i = [\mathbf{p}_{c_0}^0, \dots, \mathbf{p}_{c_k}^j]$ $j \in [0, 1, \dots, n], k \in [0, 1, \dots, m]$	✓
Structural 3D Lines	$\mathcal{S} = [\mathbf{L}^0, \dots, \mathbf{L}^j]$ $j \in [0, 1, \dots, n]$, groups of parallel lines	✓

TABLE I: Data types provided by Open-Structure Benchmark Dataset.

A. Overview of Data Types

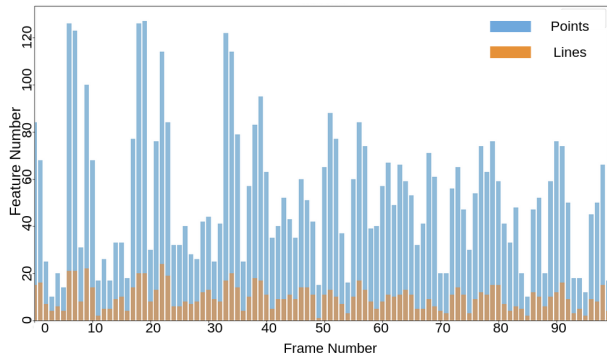
The proposed dataset is divided into two parts, the first having 16 sequences is extended from image-based datasets [14]–[16]. In contrast, the second part contains 6 sequences generated by the simulation module of our baseline. Although the sources used to build those two parts are different, the data format of those sequences is unified.

For every sequence, ground truth pose and 3D landmarks can be obtained as shown in Figure 1(a). Since 3D parallel lines are provided, those 2D line segments also have additional **structural relationships** as illustrated in Figure 1(b). Given correspondences between two frames, the relative pose is estimated based on the frame-to-frame pose computation strategy. With initial camera poses and measurements, the baseline maintains a local map to manage estimated point and line landmarks. Therefore, a map-to-frame strategy is also implemented to estimate camera pose. After obtaining observation relationships and estimating initials, the co-visibility factor graphs are constructed in the baseline, as shown in Figure 1(c), which can be optimized based on points and lines. In the proposed benchmark dataset, all those mentioned data types, **point and line measurements, structural 2D and 3D lines, 3D-2D observations, and co-visibility factor graphs**, can be directly obtained. Section III and IV, respectively, introduce the details of measurements generation and initial estimation process.

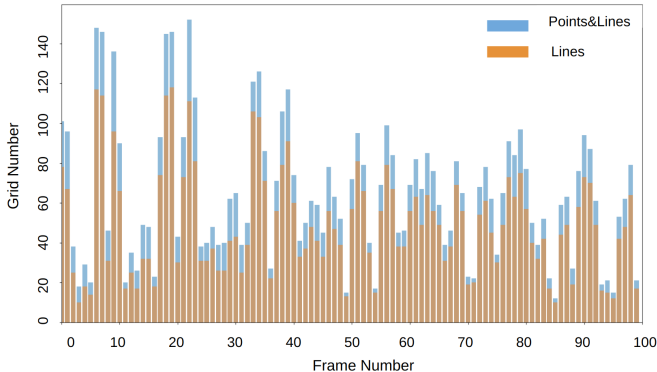
B. Statistical Analysis

Generally, qualitative characteristics, like low-/textured and non-/structured, are used to describe a sequence of visual SLAM datasets, like TUM RGB-D [14]. However, in our dataset, the portrait of each sequence can be described by quantitative values, such as the number of features of every frame, feature distributions based on occupied grids, and structural constraints.

As shown in Figure 2, each frame’s point and line measurements are satisfied. Based on those statistics, the relationships between the number of measurements and pose estimation results can be explored easily. For statistics of feature distributions, we grid each image into several cells,



(a) Statistics of feature numbers of points and lines



(b) Distribution statistics of points and lines

Fig. 2: Statistical Analysis per frame of the *sphere2* sequences.

where cell size is 10×10 . If more than one pixel is located on a cell, the cell will be regarded as occupied. Endpoints of lines are used in the statistics process. Combining the statistical results of feature numbers and feature distributions in Figure 2(a) and (b), it is not difficult to find that there are more points detected in the frame. However, the distribution is not even, indicating that many points gather together in a few parts of cells.

III. MEASUREMENTS GENERATION

This section introduces the process of measurements generation of our dataset, as introduced in Table I, the measurement of each point (or endpoint) \mathbf{p} contains the pixel position $\mathbf{p}^T = [u, v]$ and depth value d , which can be used in monocular, stereo, and RGB-D SLAM methods.

For real-world sequences (see Section III-A), our 3D scenes are generated from RGB-D sequences in ICL-NUIM [15], TUM RGB-D [14], and Tartanar [16]. Starting from those RGB-D images and ground truth poses, our real-world sequences have real space characteristics, such as scene layouts, occlusion, and robot trajectories. To increase the diversity of trajectories and observation types, simulation sequences (see Section III-B) are generated in designed trajectories and environments, where sharp/medium/slow rotational movement and rich/medium/low observations are considered to evaluate the performance of the method in

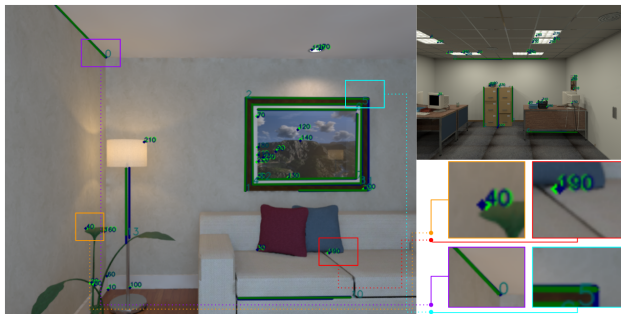


Fig. 3: Comparison in positions of detected features (blue) and measurements (green) of our dataset.

extreme cases.

A. Observation Association based on RGB-D Inputs

Given a pair of RGB-D images (F_i and D_i), ORB [22] and FLD [23] detectors are used to extract 2D points and line segments. For point features, pixel position \mathbf{p} and depth d build a point landmark \mathbf{P}_{c_i} in the i^{th} camera coordinate based on the intrinsic matrix \mathbf{K} . And \mathbf{P}_{c_i} is transformed to \mathbf{P}_w , in the world coordinate, via ground truth camera pose \mathbf{T}_{w,c_i} . Because of noise in this process, 3D projections of those correspondences will not be located at the same position in 3D space. Therefore, the 3D projections of correspondences are fused into one landmark first, and then the observation association step is to detect all observation relationships between the landmark and its observations in images. Based on the KD-Tree approach, when a new mappoint \mathbf{P}_w is generated from the current image, it will be merged into the map by considering distance and descriptor thresholds. New landmarks will be added to the map directly while existing ones will be associated with corresponding landmarks. After association successfully, the \mathbf{P}_w will be re-projected to the image to get the ground truth observations.

For each 2D line segment extracted from the image, discrete pixels lying on the line are projected to the world coordinate, similar to the process of dealing with point landmarks, with the help of depth values, \mathbf{K} and \mathbf{T}_{w,c_i} . Then, those discrete 3D points are fed to the RANSAC model to fit the endpoint-based line representation, $\mathbf{L}_w = [\mathbf{P}_w^s \ \mathbf{P}_w^e]$, in the world coordinate. The observation relationship between 2D line features and landmark \mathbf{L}_w is built in this frame. The mapline fusion approach is provided by comparing the degrees of direction vectors and line distance between existing maplines and new reconstructed ones to build the co-visible line relationship between different frames. In the mapline fusion process, the positions of line landmarks will be updated incrementally. Therefore, we only record the observed relationship in the incremental process, while the observed pixel and depth values are computed when we finish the updating process.

Although the positions of 3D point and line landmarks will be updated in the fusion process, those changes are generally small. Therefore, those re-projections of updated landmarks are still very close to the original positions computed by

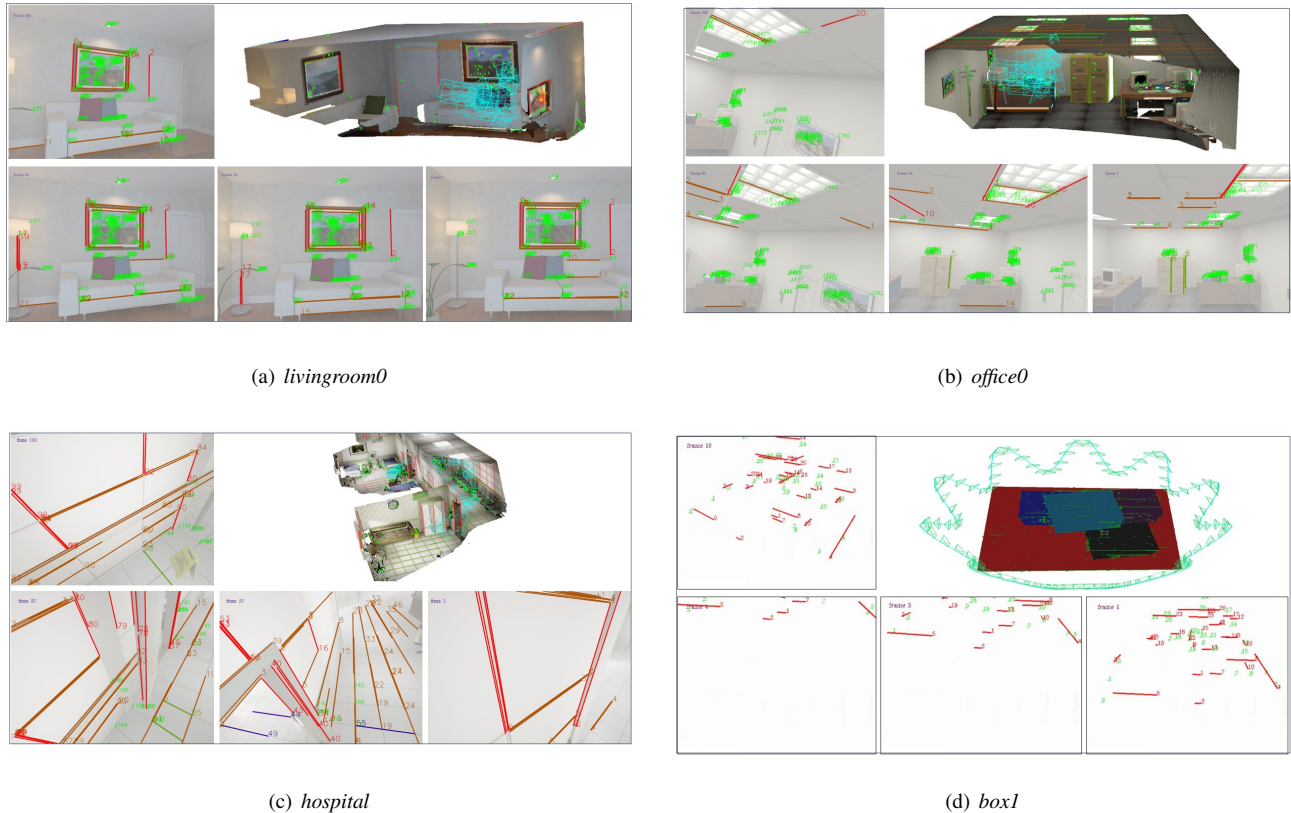


Fig. 4: Overview of trajectories, 3D model and 2D measurements of Open-Structure sequences. Point and line measurements are colored green and red, respectively. (a), (b) and (c) show reasonable feature distribution in our real-world sequences. (d) shows that simulated sequences provide diverse trajectories and observations.

feature detection methods, as shown in Figure 3, which illustrates that the data provided by our dataset shows reasonable feature distributions. Note that the observations introduced here are not actual measurements. The noise model that makes observations to measurements is introduced in Section III-C.

B. Observation Association based on Simulator

In those simulated sequences, no RGB-D images are provided. Therefore, 3D scenes and trajectories are designed first, and then sparse landmarks are distributed randomly on the surface of objects. As shown in Figure 4(d), the 3D scene is constructed by several cube boxes, and each view in the wave-shape trajectory focuses on the scene. By re-projecting those landmarks to each frame, observations can be obtained if the re-projected points and lines lie on the image planes of those views. Similarly, here, we also have to transfer those re-projection pixels to measurements by adding 2D Gaussian noise.

C. Noise Model for Measurements

Given ground truth observations, we introduce a noise model to transfer them to measurements. Based on a 3D mappoint P_w , the observe in the i^{th} image is represented as $[\hat{p}, \hat{d}]$. Therefore, the noise model [15] is to add noise in

pixel positions and depth values. For the measurement p of pixel position, it can be achieved via the $p = \hat{p} + \hat{n}$, where $\hat{n} = (\sigma_u, \sigma_v)$ is generated from 2D zero-mean Gaussian noises $\mathcal{N}(0, \sigma_s^2 \cdot \mathbf{I})$. For the depth measurement, we follow the process used in ICL-NUIM [15]. First, we build a disparity map based on the baseline model, $m = 35130$, of the Kinect sensors [24], and then add 2D Gaussian noise to the disparity map. The noised disparity map is transferred back to build the depth measurements. The process is presented as

$$d = \frac{m}{m/(\hat{d} + n_d) + \mathcal{N}(0, \sigma_d^2) + 0.5} \quad (1)$$

here σ_d is $1/6$, and n_d simulates the noise generated by the noisy disparity map. The endpoints of lines are passed to the same progress as points' to obtain measurements.

IV. BASELINE FOR INITIALS AND OPTIMIZATION

A. Initial Landmarks and Camera Poses

Given point and line measurements and observation associations, initial pose estimation and sparse mapping are implemented incrementally via the proposed baseline, as shown in Figure 5.

First, when a new group of measurements is fed to the system, a sparse 3D map based on point and line landmarks can be initialized. In the following tracking process, the

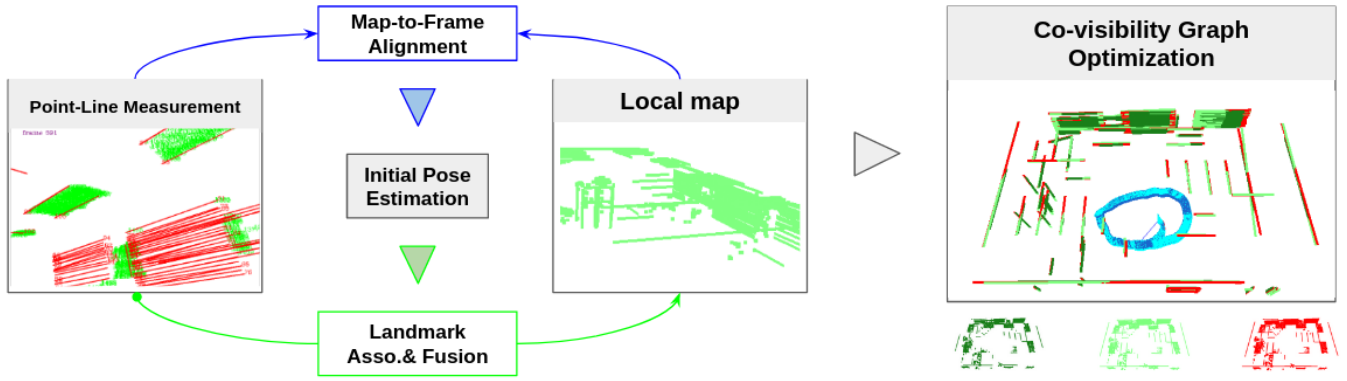


Fig. 5: The architecture of the Open-Structure baseline that reads point and line measurements directly. Initial camera poses, and a sparse map are estimated simultaneously via 3D-2D alignment and landmark fusion blocks. Co-visibility observations, initial poses, and landmarks are fed to the Co-visibility Graph Optimization module, where optimized, initial, and ground truth landmarks are highlighted in dark green, light green, and red, respectively.

initial map can be used to estimate the current camera pose \mathbf{T}_{w,c_i} based on the map-to-frame alignment module, which is implemented based on the RANSAC-based EPnP method [25]. After obtaining the initial camera pose, current frame measurements are fused to the sparse model. Those co-visible measurements are fused to update the map, while those new detections initialize new landmarks to the map.

B. Co-visibility Factor Graph Construction

Based on the estimated initial camera poses and landmarks, and measurements provided by the sequences, co-visibility factor graphs are constructed for further optimization. The vertices in this graph \mathcal{G} contain camera poses \mathcal{V}_{pose} , point landmarks \mathcal{V}_p , and line landmarks \mathcal{V}_l . To be specific, camera pose $\mathbf{T}_{w,c_i} = \begin{bmatrix} \mathbf{R}_{w,c_i} & \mathbf{t}_{w,c_i} \\ \mathbf{0} & 1 \end{bmatrix}$, where $\mathbf{T}_{w,c_i} \in SE(3)$, $\mathbf{R}_{w,c_i} \in SO(3)$ and $\mathbf{t}_{w,c_i} \in \mathbb{R}^3$. Points used in the optimization module is parametrized as $\mathbf{P}_w^k = [X^k \ Y^k \ Z^k]^T$, and line landmarks are represented in Plücker Parametrization [26] as $\mathcal{L}^k = [w_n \mathbf{n}^k \ w_d \mathbf{d}^k]$ where \mathbf{n}^k and \mathbf{d}^k are unit vectors, and the first one is the normal vector of the plane built by camera center c_i and endpoints of the k^{th} line, while the second one is the direction vector of the 3D line. Since the Plücker representation has over-parameterization issues, in the iterative optimization steps, the orthonormal method [26] \mathcal{O} is used to represent lines.

V. EXPERIMENTS

In this section, initial camera pose estimation based on Frame-to-Frame (*FtF*) and Map-to-Frame (*MtF*) strategies, point-based [1] and point-line-based [27] optimization methods are evaluated on the proposed dataset.

A. Approaches in Experiments

Optimization approaches evaluated in this paper include different optimization graph architectures and parametrization approaches. In the architecture of Co-visibility Factor

Graph (CFG), we evaluate optimization strategies used in Point BA [1] and PointLine BA [28] as listed in Table 4.

a) *Point BA*: following ORB-SLAM2 [1], Point BA makes use of the Euclidean *XYZ* form to represent point landmarks, and the loss function is based on re-projection errors between re-projected points and measurements.

Based on the point feature measurement model, the measurement of the i^{th} global point landmark $\mathbf{P}^i = [X_i \ Y_i \ Z_i]^T$ at frame c_j is represented as $\mathbf{p}_{c_j}^k = [u^k \ v^k]^T$ on the image plane, and the re-projection factor of a point feature is defined as $r_p(\mathbf{p}_{c_j}^k, \mathbf{P}^i, \mathcal{X})$ where

$$r_p(\mathbf{p}_{c_j}^k, \mathbf{P}^i, \mathcal{X}) = \mathbf{K} \overline{\mathbf{R}_{w,c_j}^T (\mathbf{P}^i - \mathbf{t}_{w,c_j})} - \mathbf{p}_{c_j}^k \quad (2)$$

here $\overline{(\cdot)}$ is to compute the normalized coordinate, \mathcal{X} shows states of camera poses. The corresponding Jacobian matrices \mathbf{J}_P and \mathbf{J}_X can be obtained respectively for updating landmarks and camera states according to Equation 2.

b) *PointLine BA*: following PL-SLAM [28], the Plücker presentation is used for re-projection error computation and the Orthonormal method is used for iterative optimization steps.

Traditionally, the process of transforming the mapline \mathcal{L}_w in the world coordinate to the camera coordinate is represented by

$$\mathcal{L}_{c_i} = \begin{bmatrix} \mathbf{n}_{c_i} \\ \mathbf{d}_{c_i} \end{bmatrix} = \mathcal{T}_{c_i,w} \begin{bmatrix} \mathbf{n}_w \\ \mathbf{d}_w \end{bmatrix} \quad (3)$$

here $\mathcal{T}_{c_i,w} = \begin{bmatrix} \mathbf{R}_{c_i,w} & [\mathbf{t}_{c_i,w}]_{\times} \mathbf{R}_{c_i,w} \\ \mathbf{0} & \mathbf{R}_{c_i,w} \end{bmatrix}$, and $[\cdot]_{\times}$ is the skew-symmetric operation.

On the image plane, the reprojected endpoints, \mathbf{p}^s and \mathbf{p}^e , of a 3D line in the camera coordinate can be obtained by

$$\bar{\mathbf{p}}^k = \mathbf{K} \bar{\mathbf{P}}^k, k \in (s, e) \quad (4)$$

here $\bar{\mathbf{P}}^k$ is a normalized 3D endpoint in the camera coordinate. Therefore, the reprojected line $\mathcal{L}^j = \bar{\mathbf{p}}^s \times \bar{\mathbf{p}}^e =$

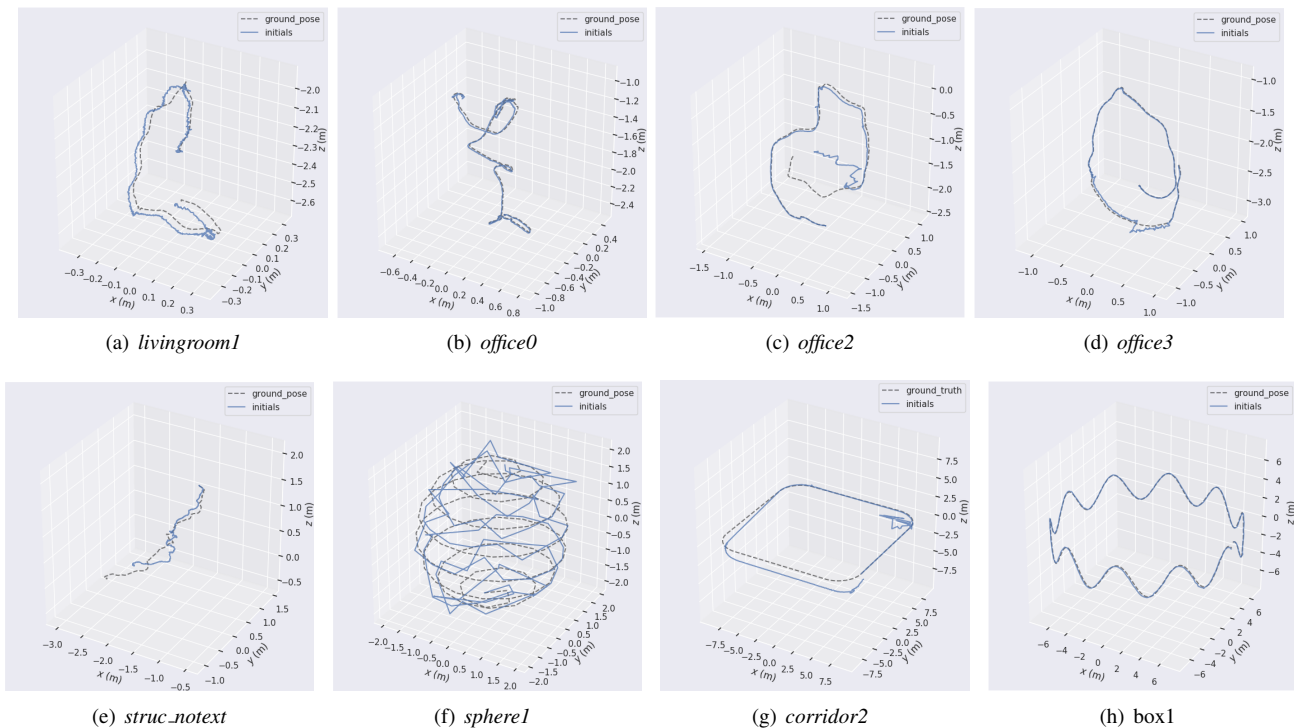


Fig. 6: Examples of ground truth (gray) camera poses and initials used in related factor graphs in Open-Structure Benchmark Dataset.

$$\mathbf{K}\bar{\mathbf{P}}^s \times \mathbf{K}\bar{\mathbf{P}}^e = \mathcal{K}(\bar{\mathbf{P}}^s \times \bar{\mathbf{P}}^e) = \mathcal{K}\mathbf{n}^j \quad [29], \text{ and } \mathcal{K} = \begin{bmatrix} f_y & 0 & 0 \\ 0 & f_x & 0 \\ -f_y c_x & -f_x c_y & f_x f_y \end{bmatrix}.$$

When the mapline \mathcal{L}_w is detected by frame c_i and c_j , we can find the 2D correspondences on related images. The error between the re-projected line \mathbf{l}^j and two endpoints, $\mathbf{p}^{j,s}$ and $\mathbf{p}^{j,e}$, of the extracted 2D line in the frame, can be written as

$$\mathbf{r}_l(\mathbf{p}^{j,s}, \mathbf{p}^{j,e}, \mathcal{L}_w, \mathcal{X}) = \begin{bmatrix} d(\mathbf{p}^{j,s}, \mathbf{l}^j) \\ d(\mathbf{p}^{j,e}, \mathbf{l}^j) \end{bmatrix} \quad (5)$$

where $d(\mathbf{p}^{j,s}, \mathbf{l}^j) = \frac{\mathbf{p}^{j,sT} \cdot \mathbf{l}^j}{\sqrt{j_0^2 + j_1^2}}$, and $\mathbf{l}^j = [l_0 \ l_1 \ l_2]^T$ is the 2D line re-projected from the j^{th} 3D mapline. $\mathbf{p}^{j,s}$ is the pixel position of the start endpoint.

B. Metrics

All experiments are carried out with an Intel Core i7-8700 CPU (with @3.20GHz). We evaluate those camera pose computation approaches on real-world and simulated sequences. Absolute trajectory errors (ATE) and relative pose errors (RPE) are used to measure the absolute and relative pose differences between estimated and ground truth motions.

C. Real World Sequences

As listed in Table II, eight real-world sequences are used to evaluate those two initial pose estimation approaches (*FtF* and *MtF*) and two factor graph optimization methods (Point-BA and PointLine-BA). In those sequences, the *MtF*

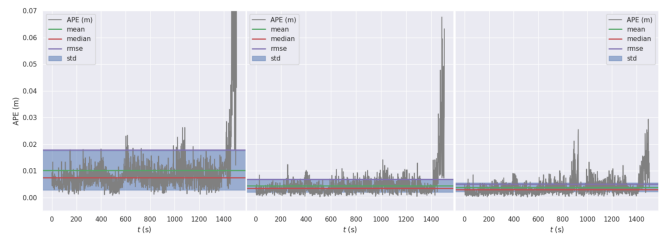


Fig. 7: APE of translation in *office0*. From left to right are results of Map-to-Frame, Point-BA and PointLine-BA methods.

tracking strategy is more robust than the *FtF* method even though the core pose computation method used in those two modules is the same algorithm (EPnP [25]). Compared with relative correspondences, *MtF* has more 3D-2D pairs for pose estimation in sequences, like *carwelding* and *office2*.

After feeding those initial camera poses estimated from the *MtF* method to a factor graph optimization module, the accuracy is continually improved in both translation and rotation. For example, in the *office3* and *stru_texture_near* sequence, the errors generated by Point-BA are reduced to one-third of the estimates of *MtF*, which shows that bundle adjustment modules have important functions in removing camera pose drift. For Point-BA and PointLine-BA factor graphs, additional co-visible connections of line observations improve the performances of point-only optimization in the *livingroom2* sequence from 0.014m to 0.007m, but when sufficient points are detected in sequences *office2* and

Sequence	Initial Pose				Co-visibility Graph Optimization			
	Frame-to-Frame		Map-to-Frame		Point-BA		PointLine-BA	
	Translation (m)	Rotation (deg)	Translation (m)	Rotation (deg)	Translation (m)	Rotation (deg)	Translation (m)	Rotation (deg)
livingroom1	0.142/0.123	0.454/0.264	0.023/0.018	0.489/0.214	0.016/0.010	0.253/0.166	0.015/0.010	0.229/0.147
livingroom2	0.253/0.206	0.732/0.201	0.081/0.039	1.607/0.185	0.014/0.006	0.528/0.125	0.007/0.005	0.235/0.106
office2	0.208/0.192	0.439/0.160	0.033/0.021	0.660/0.142	0.011/0.009	0.272/0.098	0.010/0.009	0.181/0.093
office3	0.185/0.167	0.577/0.176	0.053/0.023	1.690/0.153	0.013/0.006	0.520/0.108	0.009/0.006	0.323/0.095
hospital	0.375/0.327	0.414/0.234	0.191/0.149	0.517/0.263	0.077/0.071	0.190/0.107	0.083/0.057	0.284/0.102
carwelding	0.411/0.336	0.414/0.235	0.075/0.059	0.379/0.203	0.035/0.031	0.154/0.098	0.025/0.023	0.120/0.089
stru_texture_near	0.327/0.293	0.997/0.582	0.045/0.035	1.794/0.563	0.010/0.008	0.458/0.275	0.009/0.008	0.377/0.234
nostru_texture_near	0.883/0.727	1.130/0.642	0.183/0.064	5.756/0.881	0.044/0.030	2.914/0.319	0.033/0.031	0.582/0.252
corridor1	2.164/1.489	1.085/0.140	0.105/0.059	1.093/0.138	0.055/0.044	0.314/0.104	0.041/0.032	0.261/0.094
corridor2	0.364/0.271	0.341/0.096	0.521/0.249	02.592/0.105	0.139/0.139	0.160/0.072	0.061/0.060	0.157/0.071
box1	0.076/0.055	0.182/0.137	0.020/0.016	0.182/0.129	0.017/0.014	0.161/0.117	0.018/0.015	0.150/0.106
box2	0.739/0.576	0.289/0.178	0.096/0.030	0.399/0.177	0.028/0.015	0.331/0.143	0.020/0.014	0.239/0.130

TABLE II: Comparison of translation (APE) RMSE/MEDIAN and rotation (RPE) RMSE/MEDIAN on the Open-Structure benchmark dataset.

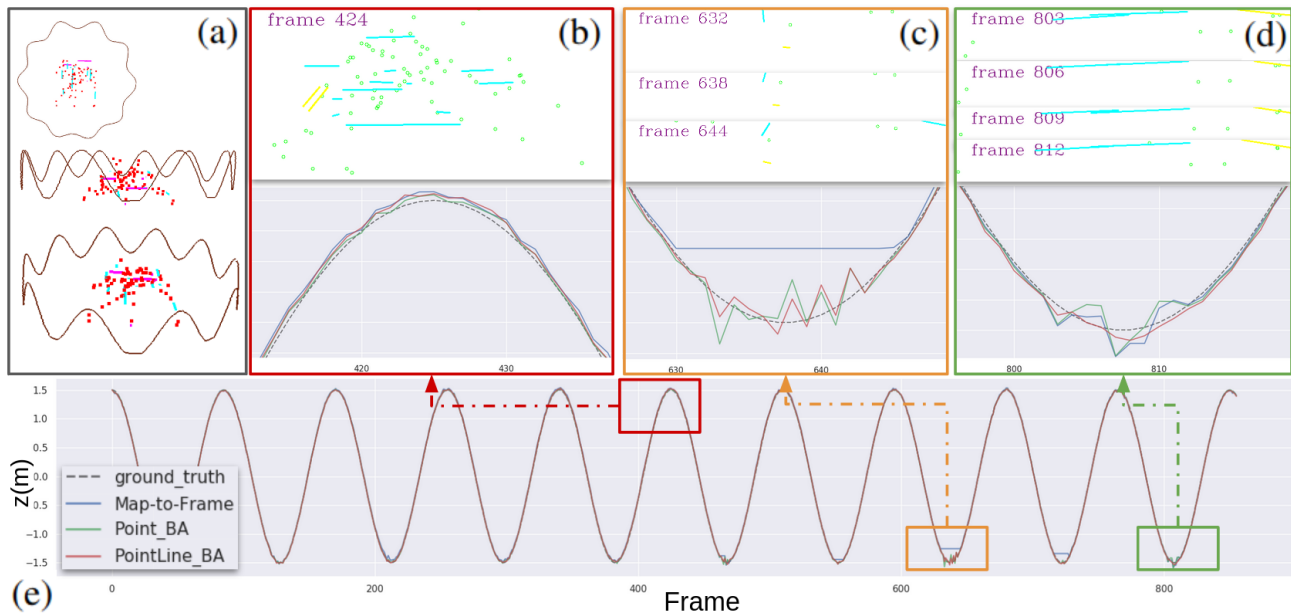


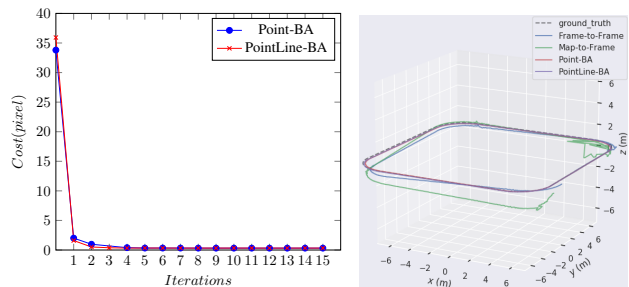
Fig. 8: Comparison in trajectory results of *MtF*, Point-BA, and PointLine-BA methods in the box2 sequence. (a) shows the simulated scene and robot trajectory from different viewpoints; (b)-(d) are zoom-in trajectories and corresponding measurements. Red rectangles show sufficient observation cases, while yellow and green rectangles highlight achieved trajectories in low-textured scenarios; (e) shows trajectories in the z-axis direction.

stru_texture_near, additional line constraints cannot improve the optimization results. In Figure 7, the pose result generated by the *MtF* method is optimized via Point-BA and PointLine-BA algorithms, where PointLine-BA achieves more robust in **std** and **rmse** metrics. More qualitative results in *office0* are provided in the supplementary video.

D. Simulation Sequences

As shown in Figure 6(f), 6(g) and 6(h), *sphere1* has more challenges in orientation estimation since the overlaps between frames are minimal, while the *corridor2* sequences are to simulate robot motions in a corridor environment, where the motions along the corridor are pure translation and sharp rotation changes in the corners. Compared with *corridor2* and *sphere1*, *box1* balances challenges in translation and rotation by following a wave-shape trajectory.

Table II shows camera pose results in four simulation sequences. The strategy of *MtF* is generally more robust than



(a) The RMSEs of Point-BA and PointLine-BA during iterative optimization

(b) Trajectory results

Fig. 9: Initials and Optimization iterations in the *corridor2* (see Figure 6(g)) sequence

the relative-frame-based pose estimation method. However, in *corridor2*, the quality of initial sparse map reconstructed incrementally is terrible, especially in the corner regions, as shown in Figure 9(b). Therefore, the *MtF* method shows a big draft at the end of trajectory. Based on the camera poses of *MtF*, the convergence steps of Point-BA and PointLine-BA are shown in Figure 9(a).

Figure 8 explores the relationships between measurements and pose computation robustness. If enough correspondences are detected in frames, like Figure 8(b), the EPnP method [25] based on 3D-2D observations achieves acceptable results. In Figure 8(c), the drafting initials are refined to better results based on factor graph optimization methods. At the same time, longer 2D lines improve the robust performance in trajectory optimization from the 803th frame to the 813th frames.

VI. CONCLUSION AND FUTURE WORKS

This paper introduces Open-Structure, a new dataset benchmark to facilitate the fair and efficient evaluation of SLAM modules, where measurements, 3D landmarks, initial camera poses, structural relationships, and co-visibility graphs can be directly obtained. The presented data preserves the real observation and occlusion relationships in real-world sequences since these sequences are extended based on RGB-D images. In simulation sequences, challenging motions and environments are designed to evaluate the performance of methods in extreme situations. For future work, new parameterization and optimization strategies are expected to be explored, especially based on the proposed structural regularities, to achieve more accurate and robust pose estimation and reconstruction performance.

REFERENCES

- [1] R. Mur-Artal and J. D. Tardós, “Orb-slam2: An open-source slam system for monocular, stereo, and rgb-d cameras,” *IEEE transactions on robotics*, vol. 33, no. 5, pp. 1255–1262, 2017.
- [2] R. G. Von Gioi, J. Jakubowicz, J.-M. Morel, and G. Randall, “Lsd: A fast line segment detector with a false detection control,” *IEEE transactions on pattern analysis and machine intelligence*, vol. 32, no. 4, pp. 722–732, 2008.
- [3] T. Qin, P. Li, and S. Shen, “Vins-mono: A robust and versatile monocular visual-inertial state estimator,” *IEEE Transactions on Robotics*, vol. 34, no. 4, pp. 1004–1020, 2018.
- [4] K. Wang, F. Gao, and S. Shen, “Real-time scalable dense surfel mapping,” in *2019 International conference on robotics and automation (ICRA)*. IEEE, 2019, pp. 6919–6925.
- [5] Y. Di, H. Morimitsu, S. Gao, and X. Ji, “Monocular piecewise depth estimation in dynamic scenes by exploiting superpixel relations,” in *Proceedings of the IEEE/CVF International Conference on Computer Vision*, 2019, pp. 4363–4372.
- [6] Y. Di, H. Morimitsu, Z. Lou, and X. Ji, “A unified framework for piecewise semantic reconstruction in dynamic scenes via exploiting superpixel relations,” in *2020 IEEE International Conference on Robotics and Automation (ICRA)*. IEEE, 2020, pp. 10737–10743.
- [7] C. Campos, R. Elvira, J. J. G. Rodríguez, J. M. Montiel, and J. D. Tardós, “Orb-slam3: An accurate open-source library for visual, visual–inertial, and multimap slam,” *IEEE Transactions on Robotics*, vol. 37, no. 6, pp. 1874–1890, 2021.
- [8] A. Rosinol, M. Abate, Y. Chang, and L. Carlone, “Kimera: an open-source library for real-time metric-semantic localization and mapping,” in *2020 IEEE International Conference on Robotics and Automation (ICRA)*. IEEE, 2020, pp. 1689–1696.
- [9] Y. Li, N. Brasch, Y. Wang, N. Navab, and F. Tombari, “Structure-slam: Low-drift monocular slam in indoor environments,” *IEEE Robotics and Automation Letters*, vol. 5, no. 4, pp. 6583–6590, 2020.
- [10] Y. Li, R. Yunus, N. Brasch, N. Navab, and F. Tombari, “Rgb-d slam with structural regularities,” in *2021 IEEE International Conference on Robotics and Automation (ICRA)*. IEEE, 2021, pp. 11581–11587.
- [11] Y. Li and F. Tombari, “E-graph: Minimal solution for rigid rotation with extensibility graphs,” in *European Conference on Computer Vision*. Springer, 2022, pp. 306–322.
- [12] J. Civera, A. J. Davison, and J. M. Montiel, “Inverse depth parametrization for monocular slam,” *IEEE transactions on robotics*, vol. 24, no. 5, pp. 932–945, 2008.
- [13] L. Zhao, S. Huang, L. Yan, and G. Dissanayake, “Parallax angle parametrization for monocular slam,” in *2011 IEEE International Conference on Robotics and Automation*. IEEE, 2011, pp. 3117–3124.
- [14] J. Sturm, N. Engelhard, F. Endres, W. Burgard, and D. Cremers, “A benchmark for the evaluation of rgb-d slam systems,” in *2012 IEEE/RSJ International Conference on Intelligent Robots and Systems*, 2012, pp. 573–580.
- [15] A. Handa, T. Whelan, J. McDonald, and A. Davison, “A benchmark for RGB-D visual odometry, 3D reconstruction and SLAM,” in *IEEE Intl. Conf. on Robotics and Automation, ICRA*, Hong Kong, China, May 2014.
- [16] W. Wang, D. Zhu, X. Wang, Y. Hu, Y. Qiu, C. Wang, Y. Hu, A. Kapoor, and S. Scherer, “Tartanair: A dataset to push the limits of visual slam,” 2020.
- [17] M. Burri, J. Nikolic, P. Gohl, T. Schneider, J. Rehder, S. Omari, M. W. Achtelik, and R. Siegwart, “The euroc micro aerial vehicle datasets,” *The International Journal of Robotics Research*, 2016.
- [18] A. Geiger, P. Lenz, C. Stiller, and R. Urtasun, “Vision meets robotics: the kitti dataset,” *The International Journal of Robotics Research*, vol. 32, pp. 1231–1237, 09 2013.
- [19] A. Gaidon, Q. Wang, Y. Cabon, and E. Vig, “Virtual worlds as proxy for multi-object tracking analysis,” in *CVPR*, 2016.
- [20] C. Forster, L. Carlone, F. Dellaert, and D. Scaramuzza, “On-manifold preintegration for real-time visual–inertial odometry,” *IEEE Transactions on Robotics*, vol. 33, no. 1, pp. 1–21, 2016.
- [21] L. Zhao, Y. Wang, and S. Huang, “Occupancy-slam: Simultaneously optimizing robot poses and continuous occupancy map,” 2022.
- [22] E. Rublee, V. Rabaud, K. Konolige, and G. Bradski, “Orb: An efficient alternative to sift or surf,” in *2011 International Conference on Computer Vision*, 2011, pp. 2564–2571.
- [23] J. H. Lee, S. Lee, G. Zhang, J. Lim, W. K. Chung, and I. H. Suh, “Outdoor place recognition in urban environments using straight lines,” in *2014 IEEE International Conference on Robotics and Automation (ICRA)*. IEEE, 2014, pp. 5550–5557.
- [24] J. T. Barron and J. Malik, “Intrinsic scene properties from a single rgb-d image,” in *Proceedings of the IEEE Conference on Computer Vision and Pattern Recognition*, 2013, pp. 17–24.
- [25] V. Lepetit, F. Moreno-Noguer, and P. Fua, “Ep n p: An accurate o (n) solution to the p n p problem,” *International journal of computer vision*, vol. 81, pp. 155–166, 2009.
- [26] A. Bartoli and P. Sturm, “Structure-from-motion using lines: Representation, triangulation, and bundle adjustment,” *Computer vision and image understanding*, vol. 100, no. 3, pp. 416–441, 2005.
- [27] Y. He, J. Zhao, Y. Guo, W. He, and K. Yuan, “Pl-vio: Tightly-coupled monocular visual–inertial odometry using point and line features,” *Sensors*, vol. 18, no. 4, p. 1159, 2018.
- [28] R. Gomez-Ojeda, F.-A. Moreno, D. Zuniga-Noël, D. Scaramuzza, and J. Gonzalez-Jimenez, “Pl-slam: A stereo slam system through the combination of points and line segments,” *IEEE Transactions on Robotics*, vol. 35, no. 3, pp. 734–746, 2019.
- [29] G. Zhang, J. H. Lee, J. Lim, and I. H. Suh, “Building a 3-d line-based map using stereo slam. *ieec transactions on robotics*,” *IEEE Transactions on Robotics*, vol. 31, no. 6, pp. 1364–1377, 2015.